JPhys Materials

PURPOSE-LED PUBLISHING™

PAPER • OPEN ACCESS

Lattice distortions and metal-insulator transition in hexagonal FeS

To cite this article: V Petkov *et al* 2026 *J. Phys. Mater.* **9** 015008

Journal of Physics: Materials

OPEN ACCESS

RECEIVED
24 May 2025

REVISED
15 September 2025

ACCEPTED FOR PUBLICATION
27 November 2025

PUBLISHED
18 December 2025

PAPER

Lattice distortions and metal-insulator transition in hexagonal FeS

V Petkov[1], J Pandey[1], A Zafar[1,*], M Jakhar[1,2] and K Beyer[3]

[1] Department of Physics, Central Michigan University, Mt. Pleasant, MI 48859, United States of America
[2] Inter-University Accelerator Center, Aruna Asaf Ali Marg, New Delhi, India
[3] X-ray Science Division, Advanced Photon Source, Argonne National Laboratory, Chicago, IL 60439, United States of America
[*] Author to whom any correspondence should be addressed.

E-mail: zafar1a@cmich.edu, petko1vg@cmich.edu and pande2j@cmich.edu

Keywords: correlated systems, lattice distortions, metal-insulator transition

Supplementary material for this article is available online

Abstract

Using total x-ray scattering and density functional theory calculations based on experimental data, we study the metal-insulator transition (MIT) in the strongly correlated system FeS with hexagonal symmetry. We find that it arises from the combined effect of static lattice distortions and antiferromagnetic ordering, while electron-electron correlations appear to play a minor role. The presence of local lattice distortions above the MIT explains well the evolution of transport and magnetic properties with changing temperature or pressure. Intrinsically, lattice distortions in hexagonal FeS act as lattice degrees of freedom that bridge competing electronic phases, thus facilitating transitions between them. The mechanism of MIT operating in h-FeS appears to be common to strongly correlated binary systems involving 3*d* transition metals, warranting further investigations on the lattice distortions-property relationship in this broad class of materials using the approach adopted here.

1. Introduction

Interactions between electronic, lattice, and spin degrees of freedom in strongly correlated systems are known to lead to the emergence of unusual physical phenomena such as metal-insulator transitions (MITs). Because of the complexity of the interactions, the driving force behind the MITs is, however, hard to reveal. In particular, it is often considered that MITs arise from electron-electron interactions, especially onsite Coulomb repulsion, that are strong enough to induce localized states and, hence, an insulating phase. MITs have also been attributed to strong electron-phonon interactions that disturb the electron mobility, leading to electron localization, without necessarily disturbing the static crystal structure. Intrinsic static distortions of the crystal structure have also been suggested to trigger MITs [1, 2]. To explore the possible scenarios, MITs are often induced by varying external stimuli such as pressure [3], temperature [4], electric [5] and/or magnetic field [6], and the response of the system is examined by advanced techniques for atomic structure determination and computational [7] tools. Using variable temperature total x-ray scattering and density functional theory (DFT) calculations based on experimental data, we show that the MIT in the strongly correlated hexagonal FeS (h-FeS) is enabled by static lattice distortions in the presence of antiferromagnetic (AFM) order, while electron–electron correlations appear to play a minor role. The distortions do not appear critical to the emergence of AFM order but seem to affect its type.

Strongly correlated h-FeS is a naturally occurring material known to exhibit unusual transport and magnetic properties. It has been found to undergo coupled magnetic [8] and structural phase transitions [9] upon changing temperature or pressure [3, 4], rendering it a topical system for studies in fields ranging from geology and space sciences to catalysis and spintronics [10, 11]. At high temperature, h-FeS is a paramagnetic metal (hereafter referred to as a PM-m phase) adopting a hexagonal space group (S.G.) $P6_3/mmc$ structure where Fe and S atoms form perfect hexagonal layers stacked along the *c* axis of the crystal lattice (figure 1 and supplemental figure S1) [9, 12–14]. Upon cooling to about $T_\beta \sim 590$ K,

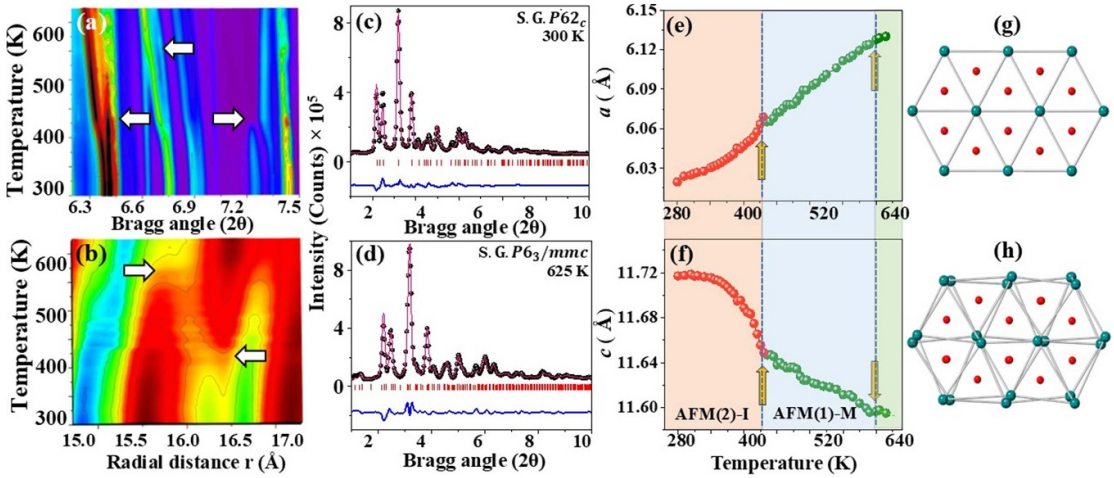

Figure 1. Intensity color maps of selected peaks in (a) XRD patterns and (b) atomic PDFs for h-FeS. Arrows indicate changes in peak intensities close to the AFM-i to AFM-m transition at $T_\alpha \sim 420$ K and AF-m to PM-m transition at $T_\beta \sim 590$ K. (c), (d) Rietveld fits (red line) to XRD patterns (symbols) obtained at 300 K and 625 K. The goodness-of-fit factors are close to 9%. The fit in (c) is based on a S.G. $P\bar{6}2c$ while that in (d) on a S.G. $P6_3/mmc$ model. Vertical red bars show the position of Bragg peaks. The residual difference (blue) is shifted for clarity. Rietveld refined hexagonal lattice parameters (e) a and (f) c as a function of temperature. The parameters below and above T_α are based on a S.G. $P\bar{6}2c$ and S.G. $P6_3/mmc$ model, respectively. In the plot, however, they are represented in the a S.G. $P\bar{6}2c$ (AFM-i cell) notation, where as $a_{AFM-i} \tilde{-} \sqrt{3}a_{AFM-m}$ and $c_{AFM-i} \tilde{-} 2c_{AFM-m}$. For both parameters, the temperature evolution exhibits clear nonlinearities at T_α and T_β (follow the vertical arrows). Projection of the ideal (g) S.G. $P6_3/mmc$ and (h) S.G. $P\bar{6}2c$ structures down the c axis of the hexagonal lattice. Fe and S atoms are in dark cyan and red, respectively. Light brown, blue and green rectangles in (e) and (f) highlight the temperature regions where hexagonal FeS appears in its AFM-i, AFM-m and PM-m phase, respectively. Per Rietveld analysis, i.e. on average, the crystal structure of the AFM-i phase is of the S.G. $P\bar{6}2c$ type while that of the AFM-m and PM-m phases is of the S.G. $P6_3/mmc$ type.

the material becomes an AFM and the character of its conductivity changes. In particular, while the resistivity, ρ, increases linearly with temperature above T_β, indicating metallic behavior, $\ln(\rho)$ has been found to gradually increase with decreasing temperature, indicating a narrow-gap semiconductor behavior. The behavior, however, can easily appear as metallic-like due to thermally activated conductivity effects. Following the widely adopted convention, hereafter we refer to this complex electronic phase as an AFM-m phase. In this phase, Fe spins are arranged in the *ab* plane of the hexagonal lattice. Upon further cooling down to $T\alpha \sim 420$ K, a spin-reorientation transition takes place where Fe spins line up with the c axis of the hexagonal axis. Concurrently, a structural phase transition takes place where the S.G. $P6_3/mmc$ symmetry is reduced to S.G. $P\bar{6}2c$ [9, 15–19]. In the structure, the alternating hexagonal layers of Fe and S atoms appear heavily distorted, as shown in figure 1 and S1 (see supplemental material). Furthermore, ρ jumps by a few orders of magnitude, indicating an insulating behavior, where, depending on the sample, the band gap has been found to be about 0.1 eV [18–20]. Hereafter, we refer to this phase as an AFM-i phase.

Recent neutron and x-ray scattering studies suggest that the MIT in h-FeS arises from a magnetically-driven phonon instability, where the AFM ordering enables the emergence of soft phonons at temperatures $T \geqslant T_\alpha$ that abruptly condense on cooling through the MIT [21]. The results seem to be supported by DFT calculations showing that no bandgap opens at T_α unless AFM order is explicitly included in the calculations. By contrast, DFT calculations of Craco *et al* [22, 23] attributed the MIT to strong electron-electron interactions. All DFT studies conducted so far, however, predict a bandgap of about 0.5 eV, which is much larger than the experimental bandgap value. As our study shows, the controversy can be resolved by conducting DFT calculations based on experimental and not DFT optimized structure data.

2. Experimental

We studied a high-quality h-FeS sample purchased from Alfa Aesar. In-house x-ray diffraction (XRD) measurements showed that it is single phase and, as expected, exhibits a S.G. $P\bar{6}2c$ type structure. Variable-temperature XRD data were obtained at the beamline 11-ID-C at the Advanced Photon Source, Argonne National Laboratory, using x-rays with an energy of 105.7 keV ($\lambda = 0.1173$ Å). The sample was kept inside a Linkam stage used to control its temperature. Scattered x-ray intensities were collected using a PerkinElmer detector while increasing the temperature from 300 K to 625 K in steps of 5 K. Two sets of XRD patterns were obtained at each temperature. One of the patterns was obtained with the

detector positioned 1500 mm away from the sample to achieve high resolution in reciprocal space. The patterns were used to perform Rietveld analysis. The other set of patterns was obtained with the detector positioned 300 mm away from the sample to reach wave vectors, q, as high as 28 Å^{-1}. The patterns were used to derive atomic pair distribution functions (PDFs) using procedures described in [24, 25]. Intensity color maps for the high-q resolution XRD patterns and atomic PDFs are shown in figure 1.

XRD intensity variations and shifts in Bragg peak positions are clearly seen at temperatures close to T_β and T_α, where the AFM-m and AFM-i phases appear upon cooling, respectively. While some Bragg peaks remain sharp in the temperature range between 300 K and 625 K, e.g. the Bragg peak at 7.2 deg., others smear, e.g. the Bragg doublet at 6.3°, producing broad diffuse scattering bands above T_α (see figure 1(a)). The observed diffuse scattering indicates the presence of a considerable local structural disorder well before the material becomes an insulator. Atomic PDFs also change considerably at temperatures close to T_α and T_β, including intensity variations and shifts in PDF peak positions. Notably, bonding distances characteristic to the low-temperature AFM-i phase and such for the high-temperature PM-m phase are seen to co-exist in the AFM-m phase, i.e. in the temperature range between T_α and T_β (e.g. see the evolution of the PDF feature at 16 Å in figure 1(b)).

3. Experimental data analysis and interpretation

To investigate the average crystal structure of h-FeS as a function of temperature, we fit the experimental XRD data collected at temperatures above T_α with a S.G. $P6_3/mmc$ structure model. XRD data collected at temperatures below T_α were fit with a S.G. $P\bar{6}2c$ type structure model. The fits were done with the help of software GSAS-II [26]. Representative fit results are shown in figures 1(c) and (d). In line with prior studies [21], the models reproduced the experimental data reasonably well. Refined values for the hexagonal lattice parameters are shown in figures 1(e) and (f). Both a and c lattice parameters are seen to exhibit a sharp change at T_α where the in-plane arrangement of Fe and S atoms (see figures 1(g) and (h)) and separation between atoms in adjacent Fe planes (Fig. S1, see supplemental material) are suggested to change profoundly. The changes in a and c parameters at $T\beta$ appear less well expressed.

Rietveld analysis, however, does not take into account the diffuse scattering component of XRD data and so may not capture well local lattice distortions in materials exhibing intrisic structural disorder. To explore the likely presence of local lattice distortions in h-FeS, we approached the experimental PDF data with the same models. Representative PDF fits are shown in figure 2. As may be expected, the S.G $P6_3/mmc$ structure model failed to reproduce the experimental PDF data obtained at 300 K (figure 2(a)), where the AFM-i phase of h-FeS appears (figure 2(a)). Surprisingly, it did not reproduce well the experimental PDF data obtained at 450 K and 550 K (figures 2(b) and (c)), where the AFM-m phase of h-FeS appears. In line with Rietveld results, the model performed much better in the case of PDF data collected at 625 K (figure 2(d)), where the PM-m phase of h-FeS appears. In line with Rietveld results, the experimental data obtained at 300 K were reproduced well by the S.G. $P\bar{6}2c$ type model (figure 2(e)). The model performed better with the PDF data obtained at 450 K and 550 K in comparison to the S.G $P6_3/mmc$ model (compare data in figures 2(f) and (g) with those in figures 2(b) and (c)), indicating that local lattice distortions of the type exhibited by the AFM-i phase persist in the AFM-m phase up to temperatures approaching T_β. Note that the quality of S.G. $P6_3/mmc$ model fits to 450 K and 550 K PDF data could not be improved beyond the level shown in figures 2(b) and (c) by adjusting the values of thermal factors alone, indicating that the observed lattice distortions in the AFM-m phase are not dynamic but largely static in character. Therefore, the anharmonic lattice instabilities, i.e. soft phonons [21], do not seem to condense abruptly at T_α. Rather, static lattice distortions appear in the AFM-m phase well above the MIT.

PDF refined values for the hexagonal lattice parameters of FeS are shown in figures 3(a) and (b). Both exhibit non-linearities at T_α and T_β. The nonlinearity at T_α does not appear as sharp as in the case of Rietveld refined lattice parameters (compare with data in figures 1(e) and (f)). This is because the PDF data obtained in the temperature range from 300 K to about 550 K are well reproduced by the same S.G. $P\bar{6}2c$ model, i.e. without enforcing a change in the crystallographic symmetry at T_α. By contrast, Rietveld analysis enforces it, suggesting an abrupt emergence of lattice distortions at T_α upon reducing temperature. Moreover, it suggests that hexagonal FeS suffers phase segregation in the MIT vicinity [21], which, as our study clearly shows, does not necessarily occur. Static displacement of Fe and S from their room temperature positions in h-FeS are shown in figures 3(c) and (d), as computed from the PDF refined structure models. As can be seen in the Figure, largely, Fe atoms undergo in-plane displacements while S atoms move both in the ab plane and along the c axis of the hexagonal lattice. The displacements accelerate at T_α and show a tendency to level off above T_β.

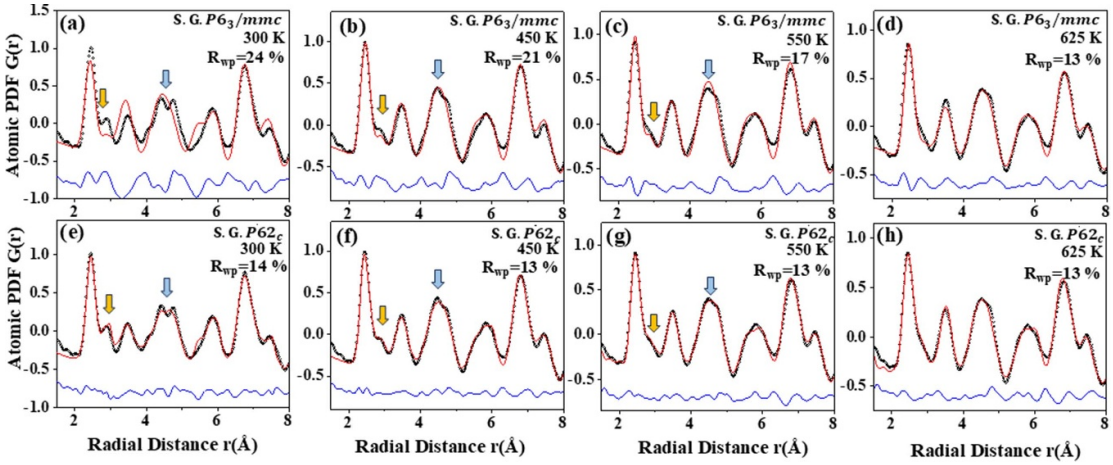

Figure 2. Fits (red line) to experimental PDFs (black symbols) for h-FeS obtained at various temperatures The fits in (a)–(d) are based on a S.G. P6$_3$/mmc model. The model does not reproduce well the PDF data obtained at 300 K, 450 K, and 550 K (a), (b), (c), in particular the strong high-r shoulder of the first PDF peak (orange arrows). It does not reproduce well the highly asymmetric PDF peak at 4.5 Å either (blue arrows). The former and latter peaks reflect interplanar Fe–Fe and various second-neighbor distances characteristic to the AFM-i phase, respectively. Notably, that shoulder and the 4.5 Å PDF peak asymmetry are hardly seen in the 625 K PDF data. Not surprisingly, the S.G. P6$_3$/mmc model fits them well (d). The fits in (e)–(h) are based on a S.G. $P\bar{6}2c$ model. The model reproduces the PDF data obtained at 300 K, 450 K and 550 K in good detail. It also reproduces the PDF data obtained at 625 K (h) as good as the S.G. P6$_3$/mmc model does (d). We believe that the latter model should be used to describe the local structure of Fe above T$_\beta$ because it has a smaller number of refinable parameters (2 lattice parameters) in comparison to the former (2 lattice parameters and 6 atomic positions).

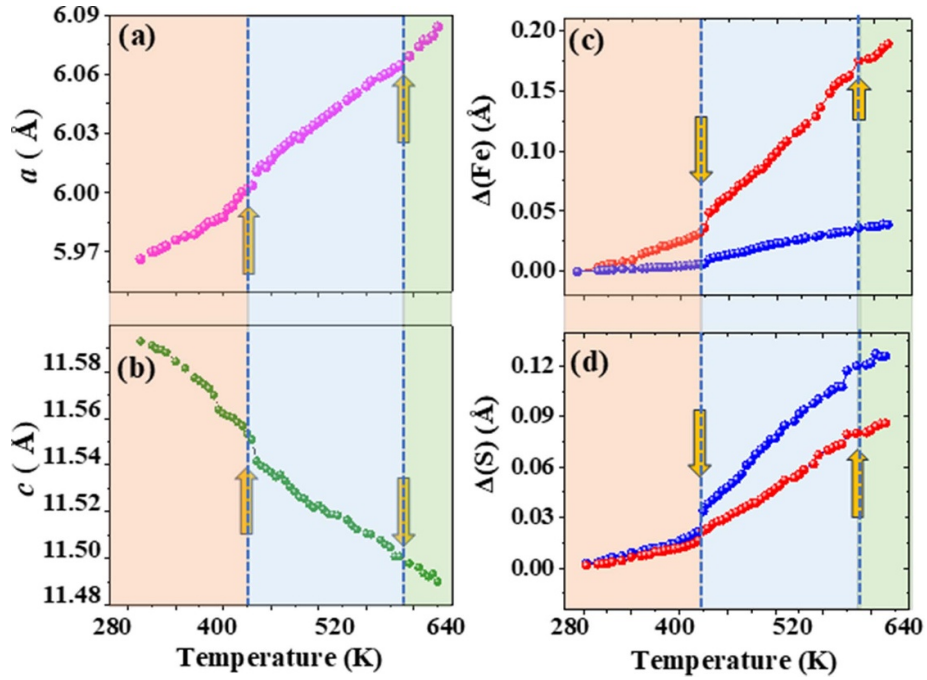

Figure 3. PDF refined hexagonal lattice parameters (a) *a* and (b) *c* for h-FeS as a function of temperature. The parameters below and above T$_\beta$ are based on a S.G. $P\bar{6}2c$ and S.G. P6$_3$/mmc model, respectively. In the plot, however, they are represented in the S.G. $P\bar{6}2c$ (AFM-i cell) notation. For both parameters, the temperature evolution exhibits nonlinearities at T$_\alpha$ and T$_\beta$ (follow the vertical arrows). Temperature evolution of the horizonal (red) and vertical (blue) static displacements for Fe (c) and S (d) atoms from their lattice positions at room temperature. Both displacements exhibit clear nonlinearities at T$_\alpha$ and T$_\beta$ (follow the vertical arrows). Light brown, blue and green rectangles highlight the temperature regions where h-FeS appears in its AFM-i, AFM-m and PM-m phase, respectively.

Hexagons of Fe atoms appearing in FeS at different temperatures are shown in figures 4(a)–(d), as derived from PDF refined models. The hexagons are seen to be very distorted below T$_\alpha$, reflecting the emergence of a variety of in-plane Fe–Fe distances. The distortion diminishes with increasing temperature and practically vanishes above T$_\beta$. The overall distortion of the hexagonal layers, Δ, computed as

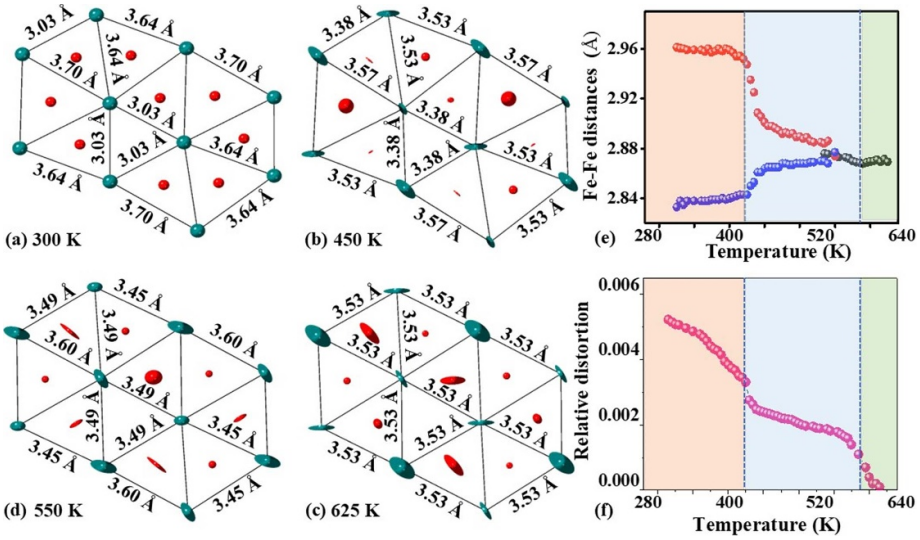

Figure 4. (a)–(d)Temperature evolution of Fe layers in h-FeS with selected Fe–Fe distances shown, as extracted from PDF refined structure models. Triangular clusters where Fe–Fe bonds are as short as 3.03 Å are seen to emerge in the AFM-i phase. (e) Temperature evolution of interplanar Fe–Fe distances. (f) Temperature evolution of the static distortion Δ, for the Fe planes in h-FeS. Fe atoms experience large dynamic disorder in the PM-m phase (c), as demonstrated by their large rms displacement amplitudes (green ellipsoids). For comparison, S atoms suffer trivial thermal disorder only, as demonstrated by their much smaller rms displacement (red ellipsoids). Light brown, blue, and green rectangles in (e) and (f) highlight temperature regions where h-FeS appears in its AFM-i, AFM-m and PM-m phase, respectively. Per PDF analysis, i.e locally, Fe planes in the AFM-m phase (450 K and 550 K) suffer static distortions of the type seen with the AFM-i phase (300 K). On the other hand, Fe planes in the PM-m (625 K) suffer dynamic structural distortions only.

$\Delta = (1/N)\ (\Sigma_n[\ (d_n - \langle d\rangle)/(\langle d\rangle)]^2)$ [27] where $< d >$ and d_n are the average and individual Fe–Fe distances in the hexagons, is shown in the figure 4(f). It is seen to decrease sharply at T_α, keep decreasing between T_α and T_β and then turn near zero above T_β, i.e. in the PM-m phase. The observed significant variation of Δ, indicates that, locally, the crystallographic symmetry also varies significantly with temperature. The evolution of distances between Fe atoms from adjacent layers is shown in figure 4(e). There are two distinct interlayer Fe–Fe distances in the AFM-i phase. The difference between the distances decreases sharply at T_α and then keeps decreasing with increasing temperature until finally disappears close to T_β where adjacent Fe layers in h-FeS appear perfectly lined up on top of each other (figure 1 and S1, see supplemental material). Overall, static lattice distortions in h-FeS appear very strong in the AFM-i phase, significant in the AFM-m phase and virtually zero in the PM-m phase where, however, Fe atoms suffer much larger root-mean-square (rms) displacements from their average lattice positions in comparison to S atoms (see the respective thermal ellipsoids figure 4(c)).

To assess the electronic properties of h-FeS, we conducted self-consistent spin-polarised DFT calculations using the generalised gradient approximation potential [28, 29], as implemented in the Vienna *ab initio* simulation package [30]. Spin-orbit interactions (usually referred to as SOC) were included in the calculations to couple the orientation of Fe magnetic moments to the crystal lattice. The plane-wave energy cutoff was set to 550 eV. Monkhorst-Pack *k*-point meshes of 10 × 10 × 6 and 16 × 16 × 10 were employed for the S.G. $P\bar{6}2c$ (24-atom unit cell) and $P6_3/mmc$ (4-atom unit cells) models, respectively. In line with results of prior studies [21], we found that, without lattice distortions, the band gap remains zero below T_α even if the on-site Coulomb interaction, U, is increased to 4 eV. When lattice distortions are included, it still remains zero unless the experimentally observed AFM order featuring a pattern of Fe spins lined up with the *c* axis of the hexagonal axis is accounted for in the calculations. The so computed electronic band structure and total density of states (DOS) for h-FeS at 300 K ($< T_\alpha$) are shown in figures 5(a) and (b). The calculations are based on an S.G. $P\bar{6}2c$ structure model ($a = 5.966$ Å and $c = 11.581$ Å) that has been refined against the respective PDF data set and not DFT relaxed, as usually done. To be more specific, they feature an effective local crystallographic symmetry, which may be related to the symmetry of the so-called crystal field, that is very much distorted (relative distortion parameter $\Delta\sim 0.004$; see figure 4(f)) in comparison to the high temperature S.G. $P6_3/mmc$ phase (relative distortion parameter $\Delta\sim 0.0005$; see figure 4(f)). The calculations predict an insulator with a bandgap of 0.16 eV, which is much closer to the experimental value of about 0.1 eV than predictions of prior DFT studies [9, 11, 21]. The DFT computed (*c*-axis aligned) magnetic moment of Fe atoms in the predicted AFM-i phase appeared close to 2.9 μ_B, which is consistent with the experimental

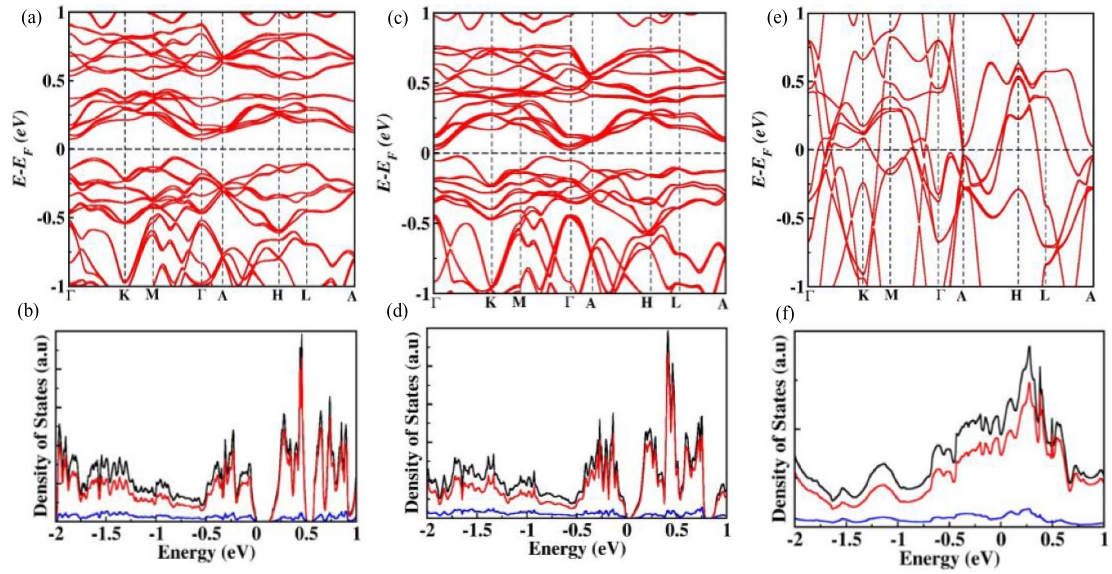

Figure 5. DFT computed (a) band structure and (b) density of states for h-FeS at 300 K. The computations are based on a PDF refined S.G. $P\bar{6}2c$ model. The material appears to be an insulator with a band gap of about 0.16 eV. DFT computed (c) band structure and (d) density of states for h-FeS at 520 K. The computations are based on a PDF refined S.G. $P\bar{6}2c$ model. The material appears to be a semiconductor with a narrow gap of about 0.04 eV. DFT computed (e) band structure and (f) density of states for h-FeS at 625 K. The computations are based on a PDF refined S.G. $P6_3/mmc$ model. The material appears to be a metal. The total DOS at the Fermi level (black line) in (b), (d) and (f), is dominated by the contribution of 3*d* electrons of Fe (red line). The vanishing contribution of S electrons to the DOS is given as a blue line.

value of 3.0 μ_B [21]. When the PDF refined structure is relaxed by spin-polarized DFT, i.e. local lattice distortions are quenched, the atomic positions and lattice parameters ($a = 5.902$ Å and $c = 11.394$ Å) appear considerably different from the experimental values, and, furthermore, the band gap is zero. Only when considerable Coulomb interactions are included in the calculations, an unrealistically large band gap of 0.53 eV opens, as illustrated in figure S2.

Results from self-consistent spin-polarized DFT calculations (SOC included) for the electronic structure of h-FeS at 520 K, which is between T_α and T_β, are shown in figures 5(c) and (d). The calculations are based on an S.G. model ($a = 6.053$ Å and $c = 11.511$ Å) that has been refined against the respective PDF data set and not DFT relaxed, thus enforcing an effective crystal field that is considerably distorted ($\Delta\sim$ 0.0012; see figure 5(f)) in comparison to the high temperature S.G. $P6_3/mmc$ phase ($\Delta\sim$ 0.0005; see figure 4(f)). In line with experimental observations, the material is predicted to exhibit a near zero-band gap characteristic to narrow-gap semiconductors. Also, in line with experimental observations [21], the DFT computed magnetic moment for Fe atoms in the predicted AFM-m phase appeared considerably smaller ($\sim$ 2.1 μ_B,) in comparison to that for Fe atoms in the AFM-i phase. The reduction in the magnetic moment value is likely due to changes in the orbital occupancy of Fe 3d states, arising from the different distortions in the crystal field in the insulator and narrow-gap semiconductor phases. Notably, as our DFT calculations show, below T_α, an AFM-m phase featuring Fe spins lying in the *ab* plane of the hexagonal lattice appears less stable energetically (by $\sim$ 0.9 eV) in comparison to an AFM-i phase featuring Fe spins oriented along the *c*-axis, indicating that the latter and not the former is the ground structure state for h-FeS, as observed by experiment.

Results from self-consistent spin-polarized DFT calculations (SOC included) for the electronic structure of h-FeS at 625 K ($>T_\beta$), featuring a noncollinear arrangement of Fe spins are shown in figures 5(e) and (f). The calculations are based on an S.G. $P6_3/mmc$ model ($a = 3.512$ Å and $c = 5.745$ Å) that has been refined against the respective PDF data set and not DFT relaxed, thus enforcing a barely distorted effective crystal field (relative distortion parameter $\Delta\sim$ 0.0005; see figure 4(f)). In line with experimental observations, the material appears to be a metal. Notably, the DOS at the Fermi level is seen to be dominated by 3d electrons of Fe atoms. Therefore, changes in near-neighbor Fe-Fe distances may be expected to modify the overlap between the 3d orbitals of Fe atoms and, hence, the transport properties of h-FeS significantly, as discussed below.

The picture emerging from our study is as follows: the crystal structure of the PM-m phase of h-FeS features near perfect hexagonal planes of Fe and S atoms (figure 4(c)) where all in-plane and interlayer

Fe-Fe distances are close to 3.53 Å and 2.88 Å, respectively (figure 4(e)). In this phase, Fe atoms suffer large rms displacements though. Nevertheless, as discussed by Goodenough [31], the near lack of static lattice distortions and related uniformity in both the in-plane and interlayer Fe–Fe distances would facilitate the emergence of a continuum of Fe–Fe π bonds [32], ultimately leading to metallic conductivity. Upon reducing temperature below 590 K, the crystal lattice distorts significantly, leading to the emergence of a variety of in-plane Fe–Fe distances (figures 4(b) and (d)) and significant reduction in the symmetry of the crystal field. Concurrently, two distinct interlayer Fe–Fe distances appear and the character of the conductivity changes from metallic to semiconductor-like. The conductivity change appears gradual with decreasing temperature below 590 K [18–20] likely because the changes in the crystal lattice, e.g. lattice parameters, bonding distances and local symmetry (figures 3 and 4), also appear gradual. When the temperature is reduced to about 420 K, the lattice distortions increase sharply (see the evolution of the parameter Δ in figure 4(f)) and triangular clusters of atoms are formed in the Fe planes. In the clusters, Fe–Fe distances appear as short as 3.03 Å while the distances between Fe atoms in adjacent clusters appear as long as 3.70 Å. Concurrently, the conductivity drops sharply, and the material becomes an insulator [18–20] likely because the continuum of overlapped 3d orbitals of nearby Fe atoms is broken due to the appearance of two very distinct interlayer Fe–Fe distances and largely disconnected planar Fe tri-clusters. The related changes in the occupancy of Fe 3*d* orbitals may also contribute to the process.

Concerning the concurrent changes in the AFM ordering pattern, Goodenough *et al* [31] proposed a scenario featuring an interplay between two contributions to the magnetic anisotropy in h-FeS. One of the contributions arises from spin-orbit interactions that tend to stabilize ordering of Fe spins along the *c* axis of the crystal lattice. The other contribution is due to dipole-dipole interactions that tend to stabilize ordering of the spins in the basal plane. The latter contribution appears to dominate the former at high temperatures, leading to an in-plane AFM ordering pattern above T_α. As our study shows, distortions of Fe planes increase sharply below T_α. This would frustrate the dipole-dipole interactions and trigger a spin-reorientation transition, promoting an out-of-plane AFM ordering pattern of Fe spins [31–33].

4. Conclusions

Our study shows that h-FeS suffers intrinsic lattice distortions involving Fe planes. The distortions are largely dynamic in the PM-m phase (no band gap) and turn static in the AFM-m phase (emerging band gap). Upon further decreasing temperature, the static distortions increase sharply leading to a spin-reorientation transition and an insulating ground state with a well-defined band gap of about 0.16 eV. Thus, the band gap in h-FeS appears to scale with the lattice (crystal field) distortions the system suffers. Their key contribution to the MIT is also demonstrated by the fact that when they are quenched by applying pressure at room temperature the material turns metallic but remains AFM [9, 12, 34, 35]. Thus, lattice distortions in h-FeS act as lattice degrees of freedom that bridge competing electronic phases, facilitating transitions between them. Cooperative mechanisms, where, in the presence of magnetic order, static lattice distortions drive MITs have been considered before. Examples include FeO [1], V_2O_3 [36], and VO_2 [37]. These similarities suggest that the mechanism of MIT operating in h-FeS is common to strongly correlated binary systems involving 3d transition metals, warranting further investigations on the lattice distortions-property relationship in this broad class of materials using the approach adopted here.

Data availability statement

All data that support the findings of this study are included within the article (and any supplementary files).

Acknowledgments

This work was supported by the U.S. Department of Energy (DOE), Office of Science, Office of Basic Energy Sciences under award DE-SC0021973. It also used resources of the Advanced Photon Source, a. U.S. DOE, Office of Science user facility operated for the DOE Office of Science by Argonne National Laboratory under Contract No. DE-AC02-06CH11357. PARAM Rudra, a national supercomputing facility at Inter-University Accelerator Centre (IUAC), New Delhi, has been used to obtain the DFT results presented in this paper.

ORCID iDs

V Petkov 0000-0002-6392-7589
J Pandey 0000-0003-3315-5335
A Zafar 0000-0001-8276-8096
M Jakhar 0000-0001-5475-0040
K Beyer 0000-0001-7490-7375

References

[1] Imada M, Fujimori A and Tokura Y 1998 Metal-insulator transitions *Rev. Mod. Phys.* **70** 1039
[2] Grüner G 1988 The dynamics of charge-density waves *Rev. Mod. Phys.* **60** 1129
[3] Petkov V, Rao T D, Zafar A, Abeykoon A M, Fletcher E, Peng J, Mao Z Q and Ke X 2022 Lattice distortions and the metal–insulator transition in pure and Ti-substituted $Ca_3Ru_2O_7$ *J. Phys. Condens. Matter* **35** 015402
[4] Kim H-S, Haule K and Vanderbilt D 2019 Mott metal-insulator transitions in pressurized layered trichalcogenides *Phys. Rev. Lett.* **123** 236401
[5] Dragoman M, Dragoman D, Modreanu M, Vulpe S, Romanitan C, Aldrigo M and Dinescu A 2025 Electric-field-induced metal-insulator transition for low-power and ultrafast nanoelectronics *Nanomaterials* **15** 589
[6] Matsuda Y H, Nakamura D, Ikeda A, Takeyama S, Suga Y, Nakahara H and Muraoka Y 2020 Magnetic-field-induced insulator–metal transition in W-doped VO2 at 500 T *Nat. Commun.* **11** 3591
[7] Godby R W and Needs R J 1989 Metal-insulator transition in Kohn-Sham theory and quasiparticle theory *Phys. Rev. Lett.* **62** 1169
[8] Shimada K, Mizokawa T, Mamiya K, Saitoh T, Fujimori A, Ono K, Kakizaki A, Ishii T, Shirai M and Kamimura T 1998 Spin-integrated and spin-resolved photoemission study of Fe chalcogenides *Phys. Rev. B* **57** 8845
[9] Ricci F and Bousquet E 2016 Unveiling the room-temperature magnetoelectricity of troilite FeS *Phys. Rev. Lett.* **116** 227601
[10] Ono S, Oganov A R, Brodholt J P, Vočadlo L, Wood I G, Lyakhov A, Glass C W, Côté A S and Price G D 2008 High-pressure phase transformations of FeS: novel phases at conditions of planetary cores *Earth Planet. Sci. Lett.* **272** 481–7
[11] Zhou G, Shan Y, Wang L, Hu Y, Guo J, Hu F and Wu X 2019 Photoinduced semiconductor-metal transition in ultrathin troilite FeS nanosheets to trigger efficient hydrogen *Nat. Commun.* **10** 399
[12] King H E Jr and Prewitt C T 1982 High-pressure and high-temperature polymorphism of iron sulfide (FeS) *Acta Crystallogr. B* **38** 1877–87
[13] Takele S and Hearne G R 1999 Electrical transport, magnetism, and spin-state configurations of high-pressure phases of FeS *Phys. Rev. B* **60** 4401
[14] Urakawa S, Someya K, Terasaki H, Katsura T, Yokoshi S, Funakoshi K I, Utsumi W, Katayama Y, Sueda Y-I and Irifune T 2004 Phase relationships and equations of state for FeS at high pressures and temperatures and implications for the internal structure of Mars *Phys. Earth Planet. Inter.* **143** 469–79
[15] Adachi K and Sato K 1968 Origin of magnetic anisotropy energy of Fe_7S_8 and Fe_7Se_8 *J. Appl. Phys.* **39** 1343–4
[16] Andresen A F, Hofman-Bang N, Bak T A, Varde E and Westin G 1960 Magnetic phase transitions in stoichiometric FES studied by means of neutron diffraction *Acta Chem. Scand.* **14** 919–26
[17] Bertaut E F 1980 On sulfides and pnictides *Pure Appl. Chem.* **52** 73–92
[18] Gosselin J R, Townsend M G and Tremblay R J 1976 Electric anomalies at the phase transition in FeS *Solid State Commun.* **19** 799–803
[19] Sakkopoulos S 1966 Antiferromagnetism and metalsemiconductor transition in iron sulfides FeS_x $1 < x < 1.25$ *J. Appl. Phys.* **59** 3540–2
[20] Hirahara E and Murakami M 1958 Magnetic and electrical anisotropies of iron sulfide single crystals *J. Phys. Chem. Solids* **7** 281–9
[21] Bansal D, Niedziela J L, Calder S, Lanigan-Atkins T, Rawl R, Said A H, Abernathy D L, Kolesnikov A I, Zhou H and Delair O 2020 Magnetically driven phonon instability enables the metal—insulator transition in h-FeS *Nat. Phys.* **16** 669–75
[22] Craco L and Faria J L B 2016 Electronic localization and bad-metallicity in pure and electron-doped troilite: a local-density-approximation plus dynamical-mean-field-theory study of FeS for lithium- ion batteries *J. Appl. Phys.* **119** 085107
[23] Craco L, Faria J L B and Leoni S 2017 Electronic reconstruction of hexagonal FeS: a view from density functional dynamical mean-field theory *Mater. Res. Express* **4** 036303
[24] Klug H P and Alexander L E 1974 *X-ray Diffraction Procedures for Polycrystalline and Amorphous Materials* (Wiley)
[25] Petkov V 1989 RAD, a program for analysis of x-ray diffraction data from amorphous materials for personal computers *J. Appl. Crystallogr.* **22** 387
[26] Toby B H and Dreele R B V 2013 GSAS-II: the genesis of a modern open-source all-purpose crystallography software package *J. Appl. Crystallogr.* **46** 544
[27] Zhou J S and Goodenough J B 2005 Universal octahedral-site distortion in orthorhombic perovskite oxides *Phys. Rev. Lett.* **94** 065501
[28] Duffy T S 2005 Synchrotron facilities and the study of the Earth's deep interior *Rep. Prog. Phys.* **68** 1811
[29] Perdew J P, Burke K and Ernzerhof M 1996 Generalized gradient approximation made simple *Phys. Rev. Lett.* **77** 3865
[30] Kresse G and Furthmüller J 1996 Efficient iterative schemes for ab initio total-energy calculations using a plane-wave basis set *Phys. Rev. B* **54** 11169
[31] Goodenough J B 1962 Cation-cation three-membered ring formation *J. Appl. Phys.* **33** 1197–9
[32] Nesbitt H W, Schaufuss A G, Bancroft G M and Szargan R 2002 Crystal orbital contributions to the pyrrhotite valence band with XPS evidence for weak Fe–Fe π bond formation *Phys. Chem. Miner.* **29** 72–77
[33] Murakami M 1961 Anisotropy of electrical conduction in iron sulfide single crystal *J. Phys. Soc. Japan* **16** 187–92
[34] K Kusaba, Syono Y, Kikegawa T and Shimomura O 1997 Structure of FeS under high pressure *J. Phys. Chem. Sol.* **58** 241–6
[35] Kusaba K, Syono Y, Kikegawa T and Shimomura O 1998 High pressure and temperature behavior of FeS *J. Phys. Chem. Solids* **59** 945–50
[36] Park J H, Tjeng L H, Tanaka A, Allen J W, Chen C T, Metcalf P, Honig J M, de Groot F M F and Sawatzky G A 2000 Spin and orbital occupation and phase transitions in V_2O_3 *Phys. Rev. B* **61** 11506–9
[37] Eyert V 2011 VO_2: a novel view from band theory *Phys. Rev. Lett.* **107** 016401